Article:
Childerhouse, T., Levano-Blanch, O., Zeng, X. et al. (5 more authors) (2024) Rapid acquisition of digital fingerprints of Ti-6Al-4V macrotexture from machining force measurement data. Materials Characterization, 207. 113550. ISSN: 1044-5803

https://doi.org/10.1016/j.matchar.2023.113550

Materials Characterization 207 (2024) 113550

Contents lists available at ScienceDirect

Materials Characterization

journal homepage: www.elsevier.com/locate/matchar

Rapid acquisition of digital fingerprints of Ti-6Al-4V macrotexture from machining force measurement data

Thomas Childerhouse [a,b,*], Oliver Levano-Blanch [a], Xiaohan Zeng [c], Joshua Taylor [a], Dennis Premoli [a], Pete Crawforth [d], Rachid M'Saoubi [e,f], Martin Jackson [a]

[a] Department of Materials Science and Engineering, University of Sheffield, Sir Robert Hadfield Building, Mappin Street, Sheffield S1 3JD, UK
[b] Element Six (UK) Ltd, Global Innovation Centre, Fermi Avenue, Harwell OX11 0QR, UK
[c] Department of Materials, University of Manchester, Royce Hub Building, Manchester M13 9PL, UK
[d] Advanced Manufacturing Research Centre with Boeing, University of Sheffield, Rotherham S60 5TZ, UK
[e] Materials & Technology Development, Seco Tools AB, SE-73782 Fagersta, Sweden
[f] Department of Mechanical Engineering Sciences, Division of Production and Materials Engineering, Lund University, Naturvetarvägen 18, 223 62 Lund, Sweden

ARTICLE INFO

Keywords:
In-process materials evaluation
Texture analysis
Crystal plasticity
Materials characterisation
Titanium alloys

ABSTRACT

Titanium alloys display anisotropic deformation properties due to the hexagonal close-packed (hcp) crystal structure of the α-phase. When subjected to localised deformation during machining, this behaviour influences fluctuations in the cutting force response of the material as the tool encounters grains of different orientations. In this research, cutting force signals acquired during face turning of Ti–6Al–4V possessing a lamellar α colony structure have been spatially mapped demonstrating the ability to identify microstructural features such as prior-β grain boundaries, grain boundary α, and α colonies. Measured cutting forces have been correlated to texture using orientation information acquired from large area EBSD analysis. A relationship between the misalignment of the crystallographic ⟨*a*⟩ slip vector with respect to the cutting direction and the passive cutting force response has been established, demonstrating a rise in cutting forces as this misalignment is increased. This novel approach to in-process materials evaluation offers manufacturers the potential of a powerful digital quality assurance tool, with the results presented here demonstrating the possibility for rapid characterisation of entire component surfaces, revealing microstructural features, and inferring the crystallographic orientation of macrotextured regions in Ti–6Al–4V.

1. Introduction

The measurement of cutting forces during machining operations has become a commonly implemented practice to evaluate cutting tool performance [1,2], optimise process parameters [3], and assess the dynamic stability of the process [4,5]. Force measurements are typically considered as scalar quantities and are used to asses the effects of changes in process parameters on the cutting force magnitude imparted by the interaction between the tool and workpiece. When analysing cutting forces, heterogeneous and anisotropic deformation characteristics of the workpiece material are rarely considered and materials are instead often regarded to possess homogeneous and isotropic properties. For machining polycrystalline materials this approach is often appropriate, as stresses typically operate over an interaction volume containing a sufficient number of grains, such that the anisotropic effects arising from the crystallographic orientation of individual grains are averaged out. However, in certain polycrystalline materials, such as coarse grained Ti–6Al–4V, which can possess large colonies of similarly orientated α lamellae, the effects of crystallographic orientation on the cutting force response becomes more pronounced [6].

For large scale titanium alloy rotative aeroengine components, assurance that microstructural properties, such as grain size and crystallographic texture, meet specification criteria is critical to ensure their safe operation. Of particular importance can be the presence of macrozones, microtextured regions possessing similar crystallographic orientation, developed through the growth of α colonies [7]. Unfavourable orientation combinations between neighbouring macrozone pairs has been shown to promote early crack initiation under cold-dwell fatigue

* Corresponding author at: Department of Materials Science and Engineering, University of Sheffield, Sir Robert Hadfield Building, Mappin Street, Sheffield S1 3JD, UK.
E-mail address: thomas.childerhouse@e6.com (T. Childerhouse).

https://doi.org/10.1016/j.matchar.2023.113550
Received 15 September 2023; Received in revised form 21 November 2023; Accepted 6 December 2023
Available online 12 December 2023

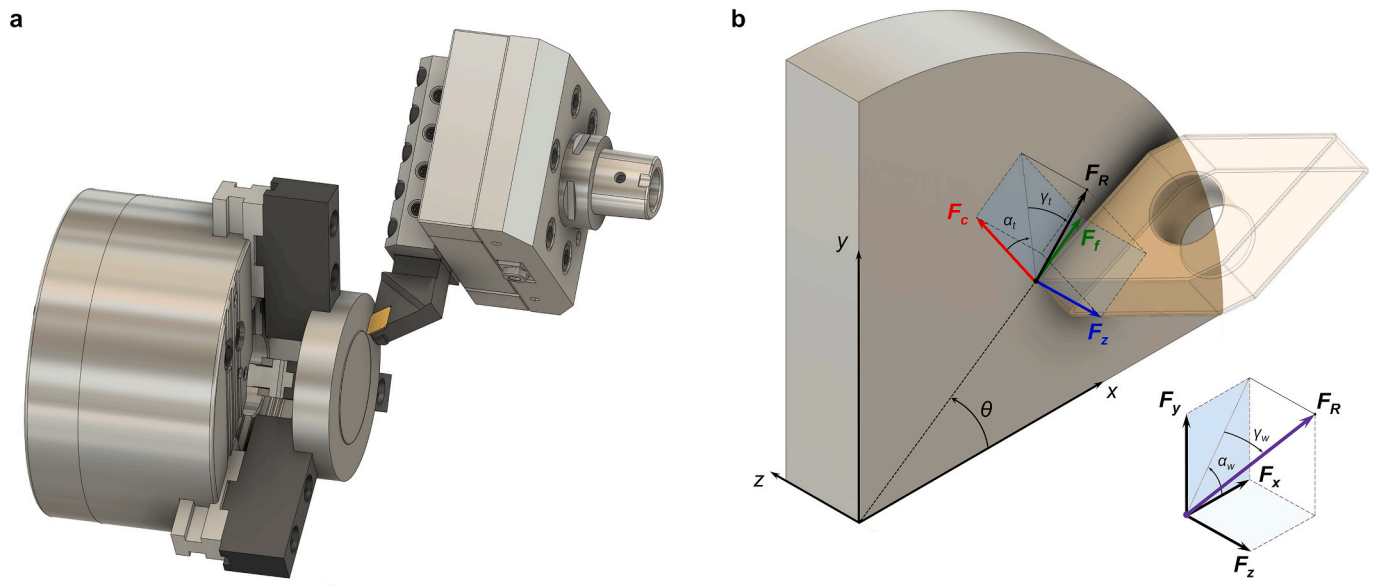

Fig. 1. Spatial mapping of machining force data for characterisation of microstructral features. **a,** Schematic detailing the force measurement hardware integrated in a face turning operation. **b,** Schematic illustrating the tool/workpiece contact indicating the principle force directions measured in the coordinate system fixed to the rotating tool (F_f, F_c, and F_z) and the coordinate system fixed to the workpiece (F_x, F_y, and F_z).

loading conditions due to dislocation pile-up at these interfaces [8,9]. Cold-dwell initiated fatigue failure of titanium alloy components, such as fan and compressor discs, is a major concern for aeroengine manufacturers. Therefore, precautions are taken by implementing time consuming and costly quality assurance methods to attempt to identify potentially deleterious microstructural features. Current methods involve performing EBSD analysis of representative sample material. Destructive evaluation techniques like these are however problematic, as they require a statistical extrapolation of results obtained from small sample sizes to predict the condition of very large components. Therefore, the development of non-destructive evaluation (NDE) techniques offering the ability to rapidly characterise large component areas would be highly beneficial from a safety standpoint and would improve the efficiency of quality assurance.

Due to the extensive machining requirements for titanium alloy aeroengine components, the possible application of cutting force measurement analysis methods to predict workpiece crystallographic texture by exploiting the relationship between crystal anisotropy and cutting force, seems both theoretically possible and readily implementable in-line with existing machining operations. The state-of-the-art in the use of cutting force analysis for materials characterisation has been predominantly performed using data acquired during face turning, using a configuration similar to that shown in Fig. 1. Due to the single point of contact between the tool and workpiece, it is possible to transform cutting force data acquired in the time domain into the spatial domain of the newly machined surface, by predicting the spatial location of each data point along the tool/workpiece contact path. Crawforth et al. [10] demonstrated that spatial mapping of resultant cutting force measured during face turning of Timetal Ti–54M revealed high force regions located at four poles of the billets cross section, which were attributed to regions subjected to higher levels of strain during primary forging. These findings highlighted that underlying crystallographic texture and microstructural variations across the billets cross section could be revealed from the cutting force response of the material. Microstructural characterisation through analysis of cutting forces was developed further by Suárez-Fernández et al., who demonstrated that spatial mapping of cutting force data could reveal prior-β grains (of diameter ~ 1360 μm) in Ti–17 [11]. Under the cutting conditions employed, the size of the interaction volume of machining stresses acting in the tertiary shear zone was shown to be below that of the prior-β grain size. The material investigated possessed a basketweave α grain structure which was found to promote a force response linked to the average crystallographic orientation of α-variants nucleated within each prior-β grain. In subsequent research, the same authors demonstrated that it was possible to distinguish between Ti–6246 workpieces in the as-forged, mill-annealed, solution treated and aged, and β-annealed conditions, from fluctuations in their cutting force response [12].

In micro-machining the cutting edge radius is frequently on a size scale approaching that of an individual grain of the workpiece material. Coupled with the need to machine at very low feed rates, often in the order of several μm, due to the delicacy of tooling and component features, machining stresses can act over a scale similar to that of individual grains. This has been shown to introduce a size effect, whereby crystallographic orientation can influence periodic effects on the machining response [13]. Studies on the effects of crystal anisotropy during micro-machining of single-crystal fcc materials including copper and aluminium have been carried out revealing variations in cutting force, specific cutting energy, shear stress/angle, and surface roughness as a result of altering crystal orientation with respect to the cutting direction [14,15]. Various single-crystal plasticity models have been developed to understand these effects by modelling the relationship between cutting direction and crystal orientation. Early models by Sato et al. [16], attempted to predict shear angle during machining of single crystal aluminium using a Schmid factor approach [17] by calculating the critically resolved shear stress (CRSS) along slip planes from experimentally measured cutting forces. Active slip planes were identified by those where the CRSS exceeded a critical threshold value, which was used to estimate the shear angle by resolving the sum of the active slip vectors to determine the resultant slip vector along the cutting direction. The limitations of this approach, highlighted by Demir et al. [18], was the assumption of a principle stress state of the material at the shear plane and a proportional relationship between the CRSS and the amount of slip, which is not in agreement with Schmid theory [17].

Lee and Zhou [19] applied a modified Taylor-based model to analyse shear angle due to variation in the cyrstallographic cutting direction, which was compared to experimental results acquired during turning of single crystal β-brass (bcc). Correlations with a Texture Softening Factor, derived by the modified Taylor factor, revealed better correlation agreement between the predicted shear angle and crystal orientation of the material when compared to the Schmid factor approach employed in

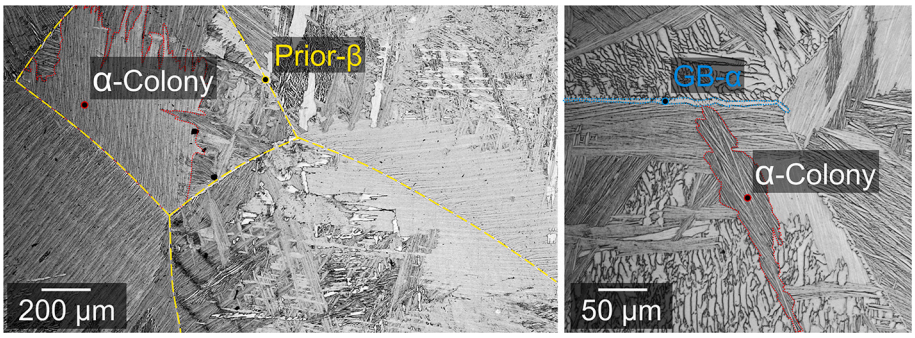

Fig. 2. Optical light micrographs showing the transformed prior-β, lamellar α colony microstructure of the FAST Ti–6Al–4V workpiece material.

the original study by Ueda and Iwata [20]. Yuan et al. [21], applied a similar method to predict cutting forces during turning of single-crystal aluminium and copper (fcc), demonstrating correlations between crystal orientation, cutting force fluctuations, and surface roughness. Taylor-based models predict the shear angle based on the shear plane which requires the minimal crystallographic work for slip activation for the given crystal orientation [18]. These approaches have been expanded upon to include the effects of frictional contact between the rake face and chip, further improving their ability to predict orientation effects on specific cutting energy in orthogonal cutting of single-crystal materials [18,22–24]. It is notable that Taylor-based methods are rate-insensitive and therefore, do not account for cutting speed or strain rate hardening. For materials such as titanium alloys, which display highly strain rate dependent chip formation behaviour, which results in adiabatic shear band formation, the validity for the application of such models is limited. Furthermore, these models do not consider the temperature dependence of flow stress, or the effects of the size of the cutting edge radius and deformation of material in the tertiary shear zone. More recently, Demir and Mercan [25] proposed a physics-based single-crystal plasticity model for fcc materials, accounting for strain rate, temperature, and length scale strain hardening effects. Compared to Taylor-based models, this approach demonstrated improved predictions of cutting force fluctuations due to crystal anisotropy. Similar to previous models, size-effects of the cutting edge radius were unaccounted for and would require further refinement of the model. To this author's knowledge, no similar models have been developed for hcp metals, such as titanium, with the main challenges being capturing the complex chip serration mechanics that occurs during chip formation, which has been shown to fluctuate depending on α orientation [6].

In micro-machining of polycrystalline materials, the influence of texture on the machining behviour of hcp material was studied by Kieren-Ehses et al. [13], who performed orthogonal cutting experiments on commercially pure titanium. Measured fluctuations in cutting forces were shown to correlate with the location of grain boundaries. Based on texture analysis performed using polarised light microscopy, a relationship between the resistance to slip deformation resulting from individual grain orientation and cutting force was demonstrated. Forces in the cutting direction were shown to be lowest for grains where the (0001) plane was most closely aligned parallel to the machined surface, with this orientation facilitating low resistance to basal $\langle a \rangle$ slip due to alignment of the crystal a-axis with the cutting direction. Analysis of the machined surface topography revealed deviations in surface height also corresponding to grain boundary locations, which was attributed to variations in elastic recovery at neighbouring grains due to crystal anisotropy.

This research presents further developments for the characterisation of microstructural features of polycrystalline Ti–6Al–4V through the analysis of cutting force measurements acquired during face turning experiments. Large area EBSD orientation mapping has been performed following machining and the crystallographic texture has been correlated to variations in the cutting force response. The findings presented

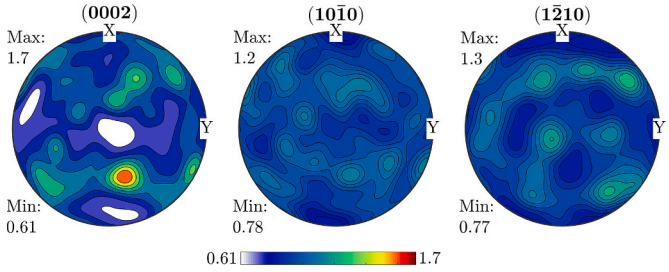

Fig. 3. Basal {0002}, Prismatic {10$\bar{1}$0} and {1$\bar{2}$10} pole figures corresponding to the FAST Ti–6Al–4V workpiece machined surface. The z-direction is in the centre of the pole figure corresponding to the powder compression direction during sintering.

demonstrate that the measurement and analysis of fluctuations in cutting forces, due to changes in the crystallographic cutting direction as the tool moves across grain boundaries, has the potential to provide a method to both characterise the microstructure and infer the crystallographic texture of the workpiece material.

2. Methods

2.1. Workpiece material

The workpiece material used for this study was produced by Field Assisted Sintering Technology (FAST), a solid state powder metallurgy process which uses pulsed DC electric current for direct heating of a graphite mould assembly and the sample through the Joule heating effect [26]. The process facilitates a high level of control over the microstructural properties of the sample due to the accurate and rapid control over processing temperature. Discs of 80 mm diameter were consolidated using Ti–6Al–4V pre-alloyed powder using a FCT Systeme GmbH Type HP D 25 system. Processing was performed under vacuum at a dwell temperature of 1300 °C for an 80 min duration under an applied pressure of 35 MPa. The sample was then allowed to cool to ambient conditions.

The microstructure of the workpiece material is shown in Fig. 2. A lamellar colony structure of clusters of parallel primary α plates can be distinguished along with a continuous α layer at prior-β grain boundaries. The size of α colonies can be seen to vary from small clusters to colonies approaching the size of prior-β grains. The microstructure is typical of that developed in β-annealed Ti–6Al–4V following slow cooling from above the β-transus temperature [27]. Processing the sample at temperature conditions above the β-transus temperature and for an extended dwell duration was carried out to produce a workpiece with a fully β-transformed microstructure with large prior-β grains containing similarly orientated α colonies [28]. Using material featuring such a coarse prior-β grain size has aided the analysis, demonstrating the microstructural features that can be revealed from the cutting force

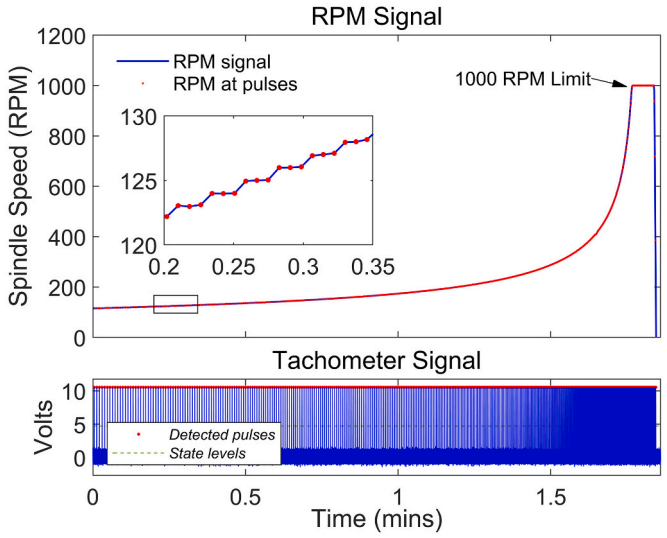

Fig. 4. An example of an optical tachometer signal recorded during the face turning operation showing the corresponding calculated spindle speed.

information. Additionally, the large size of macrotextured regions developed has reduced the possible error influenced by spatial misalignment between EBSD orientation and cutting force data.

Pole figures corresponding to the FAST Ti–6Al–4V workpiece machined surface are provided in Fig. 3 and show a highly random texture with no preferential alignment to any reference axis including the axial powder compression z-direction.

Preparation of the workpiece was performed prior to acquisition of the force data presented in this study. This involved face turning the disc with the workpiece mounted in-situ on the machine tool to remove the as-sintered surface finish and achieve concentric and parallel alignment between the tool and workpiece.

2.2. Machining operation

The cutting force data used for the analysis presented in this study was acquired during a face turning operation performed using a DMG Mori NLX2500 CNC turning centre. To generate a force signal influenced predominantly by the effects of changes in the workpiece's crystallographic texture, cutting parameters were selected to emphasise the forces associated with workpiece deformation in the tertiary deformation zone compared to those associated with frictional and shearing effects in the primary and secondary deformation zones. This involved selecting a tool (Seco Tools DCMT11T304-F1 CP500) with an unworn cutting edge featuring a large edge radii (30 μm) with respect to the uncut chip thickness, 100 μm. This increases the ratio of the uncut chip thickness subjected to a local negative rake angle, thereby causing it to be deformed beneath the cutting edge. The axial depth of cut, a_p was set at 0.1 mm. In combination with the relatively low feed rate, f_n this resulted in a small uncut chip area and therefore, a reduction in the forces associated with chip formation in the primary shear zone compared to more aggressive machining processes. The cutting speed, V_c was also set to a relatively low value of 30 m.min^{-1} to reduce any tendency for dynamic instability of the process.

The face turning operation was performed using a G96, constant V_c, command, whereby the demanded spindle speed increases as the tools radial position approaches the centre of the workpiece. To ensure the angular position of the force data could be accurately mapped spatially, an optical tachometer was included in the measurement setup to record a voltage pulse once per spindle revolution, synchronous to the force measurement. An example of a tachometer signal is provided in Fig. 4, showing the voltage pulse and corresponding calculated spindle speed. The spindle speed can be seen to increase exponentially until it reaches the predefined 1000 RPM limit. It was observed from these measurements that the spindle displayed a stepping behaviour whereby the spindle speed would be rounded to whole integers of the RPM. This behaviour is presumed to be an effect of the control system implemented by the manufacturer and is not expected to have had a significant influence on the measured forces due to the low corresponding variation in V_c (<0.1 m.min^{-1}).

2.3. Cutting force measurement and analysis

Cutting forces were measured in the F_c, F_f, and F_z directions (Fig. 1) using a Kistler 9129AA piezoelectric multicomponent dynamometer employing a data acquisition rate of 25.6 kHz. Under the cutting parameters employed, the spatial data point resolution was 19.7 μm in the circumferential direction and 100 μm (equivalent to f_n) in the radial direction.

According to the manufacturers specifications, the dynamometer featured a sensitivity <10 mN and a natural frequency <4.5 kHz. Signal conditioning was performed using a Kistler Type 5070A multichannel charge amplifier which performed real time amplification of the piezoelectric charge signal, converting this to a proportional voltage which was recorded directly into MATLAB for post-processing using a NI-9178 cDAQ through a NI-9234 input measurement module.

During the face turning operation, the tool tip traces an achemedian spiral across the face of the workpiece material towards the centre. For mapping the spatial coordinates of each force data point position along this path, the following equations can be used to determine the instantaneous radial, $r(t)$ and angular, $\theta(t)$ position of the tool in polar coordinates:

$$r(t) = r_0 - f_n \dot{\theta}(t).\mathrm{d}t \tag{1}$$

$$\theta(t) = \theta_0 + \dot{\theta}(t).\mathrm{d}t \tag{2}$$

where, r_0 is the radius of the workpiece, $\dot{\theta}(t)$ is the instantaneous rotational speed of the workpiece and θ_0 is the angular position of initial tool engagement. To perform the spatial mapping of the force data, the radial tool position, $r(t)$ was determined using the programmed value for f_n, therefore assuming no positional error of the linear feed drive of the CNC machine tool. The angular position of the tool, $\theta(t)$ however, was determined based on the tachometer sensor measurement with linear interpolation of the spindle speed values between the pulse readings acquired each spindle revolution.

Translation of the cutting force measurements from the coordinate system fixed to the cutting tool (F_c, F_f, and F_z) to the specimen reference frame (F_x, F_y, and F_z) can be performed using the transformations provided in Eq. 3.

$$\begin{bmatrix} F_x \\ F_y \\ F_z \end{bmatrix} = \begin{bmatrix} cos(\theta) & sin(\theta) & 0 \\ sin(\theta) & -cos(\theta) & 0 \\ 0 & 0 & 1 \end{bmatrix} \begin{bmatrix} F_f \\ F_c \\ F_z \end{bmatrix} \tag{3}$$

2.4. Orthogonal cutting model

To further understanding the machining induced stress interaction with the workpiece material, a thermo-mechanically coupled finite element (FE) 2D orthogonal cutting model was developed in DEFORM using the Calamaz modified Johnson-Cook constitutive material model [29]. Cutting parameters for V_c, f_n, cutting edge radii, and insert rake/clearance angle were set at 30 m.min^{-1}, 0.1 mm, 30 μm, 7°, and 15°, respectively and were representative of those used in the face turning experiments. Workpiece material properties were taken from the DEFORM material library for Ti–6Al–4V using flow stress data developed by SFTC based on work by Umbrello [30], Lee and Lin [31], and El-Magd and Treppmann [32–34] and the damage model by Umbrello

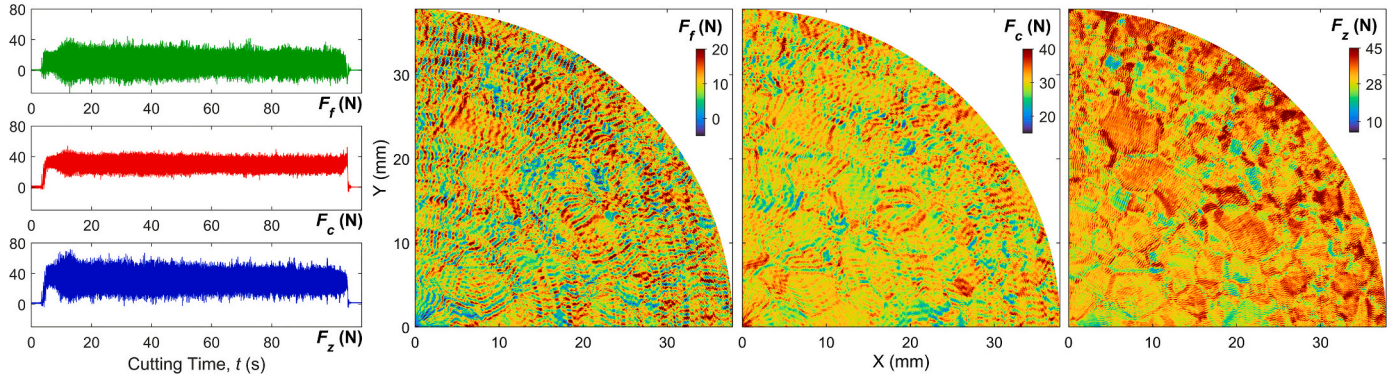

Fig. 5. Cutting force signals (F_f, F_c, and F_z) shown in the time domain acquired during face turning of the Ti–6Al–4V workpiece and the corresponding forces mapped spatially over the machined surface.

[30]. Tool material properties were also taken from the DEFORM library for WC using values for Young's modulus, poisons ratio, density, and thermal conductivity of 650 GPa, 0.25, 15,700 kg/m^3, and 59 W/mk, respectively. Thermo-mechanical contact between the tool and workpiece were modeled with heat transfer and coulomb friction coefficients of 4×10^4 W/m^{2}K and 0.2, respectively and an assumption that 90% of mechanical work and frictional energy was converted to heat equally partitioned between the workpiece and the cutting tool was applied.

2.5. EBSD analysis

Crystallographic texture information of the workpieces was obtained by performing EBSD analysis of the machined surface following the face turning operation used to acquire cutting force data. Metallographic preparation of the machined surfaces involved progressive grinding with SiC abrasive paper, followed by chemical/mechanical polishing with a solution of 90% colloidal silica (0.05 μm) and 10% H_2O_2 (30% w.v^{-1}). The specimen thickness was measured both prior and following metallographic preparation indicating a removal depth <5 μm suggesting minimal removal of microstructural features detectable during the cutting force measurement.

EBSD analysis was carried out using a ThermoFisher Apreo C FEG-SEM equipped with an Oxford Instruments CMOS Symmetry detector and Aztec 6.0 acquisition software. The accelerating voltage, current, tilting angle, and working distance were 20 kV, 26 nA, 65°, and 27 mm, respectively and a step size of 20 μm was chosen. Scans were operated in the "speed 2" mode, producing EBSD patterns in 156 × 128 pixels resolution. Patterns were refined with 60 Hough space resolution and 11 band detection. For the internal 34 mm specimen diameter, scanning was repeated using an increased exposure time and frame averaging to achieve higher contrast on Kikuchi patterns, thus, a better index rate. The EBSD data sets acquired from the scans of the entire sample surface and internal 34 mm diameter were combined into a single data set, achieving an indexing rate >76% over the entire sample area. Post-processing and further analysis of the orientation data was then carried out using the MTEX toolbox in MATLAB [35].

3. Results and discussion

The results in the following section have been divided into those regarding identification of microstructural features and prior-β grain boundaries from spatially mapped cutting force data, followed by a discussion regarding the crystallographic cutting force relationship. Finally, cutting force maps corresponding to workpieces featuring finer grain sizes are presented to demonstrate the technique's capabilities for characterising materials with different underlying microstructures.

Mapped cutting force data acquired in the F_f, F_c, and F_z directions during the face turning experiments is provided in Fig. 5. In the analysis presented throughout this study, the data has remained unfiltered and any processing steps have been outlined in the experimental method. Comparing the data acquired in the three force component directions, shows that microstructural features can be distinguished most clearly from forces in the F_z direction. This signal displays higher contrast information at grain boundaries when compared to F_f and F_c. Observations of the time domain signals indicates that F_z is of a higher magnitude and displays greater levels of fluctuation than F_f and F_c. The observation that higher contrast microstructural information can be distinguished from the map of the F_z signal suggests that fluctuations in cutting force in this direction are more directly influenced by anisotropic deformation behaviour and the local crystallographic orientation of the workpiece. Whereas F_f and F_c are more closely associated to the effects of chip formation in the primary shear zone and frictional contact at the chip/rake face interface in the secondary deformation zone, F_z is more directly associated with deformation taking place in the tertiary shear zone. This occurs through a phenomena known as ploughing [36], whereby deformation of the workpiece is induced as it is squeezed beneath the cutting tool. Ploughing is promoted by stagnation and separation of the flow of the uncut chip ahead of the tool as it experiences a local negative rake angle due to the radius of the cutting edge. This causes a portion of the uncut chip to flow beneath the tool, rather than forming the chip [37]. This suggests that to characterise the microstructure effectively, localised deformation induced through ploughing is required to generate a cutting force signal containing sufficient information related to changes in the crystallographic cutting direction as the tool passes over grain boundaries.

From the F_f and F_c maps (Fig. 5), radial banding can be observed, indicating regular periodic fluctuation in cutting force. Based on Fourier analysis of the signal in the frequency domain, this banding occurs at an approximate frequency of 2 kHz. It is believed that these fluctuations in force correspond to periodic chip serration resulting from the effects of adiabatic shear banding during chip formation, which is typically observed in Ti–6Al–4V [6]. Further discussion related to these observations are provided later in this article.

3.1. Microstructural feature identification

To evaluate the characterisation capabilities attainable from analysis of the cutting force data, a comparison between a map of the F_z force component and EBSD orientation data, presented as an inverse pole figure (IPF) map, is given in Fig. 6. The magnitude of F_z can be seen to shift as the tool moves across prior-β grain boundaries making it possible to distinguish the the prior-β grain structure at the machined surface of the specimen. These changes in cutting force can be attributed to variations in the crystallographic cutting direction as the tool encounters grains of different textures and therefore, changes in their resistance to slip deformation and tool motion. In titanium alloys processed above the

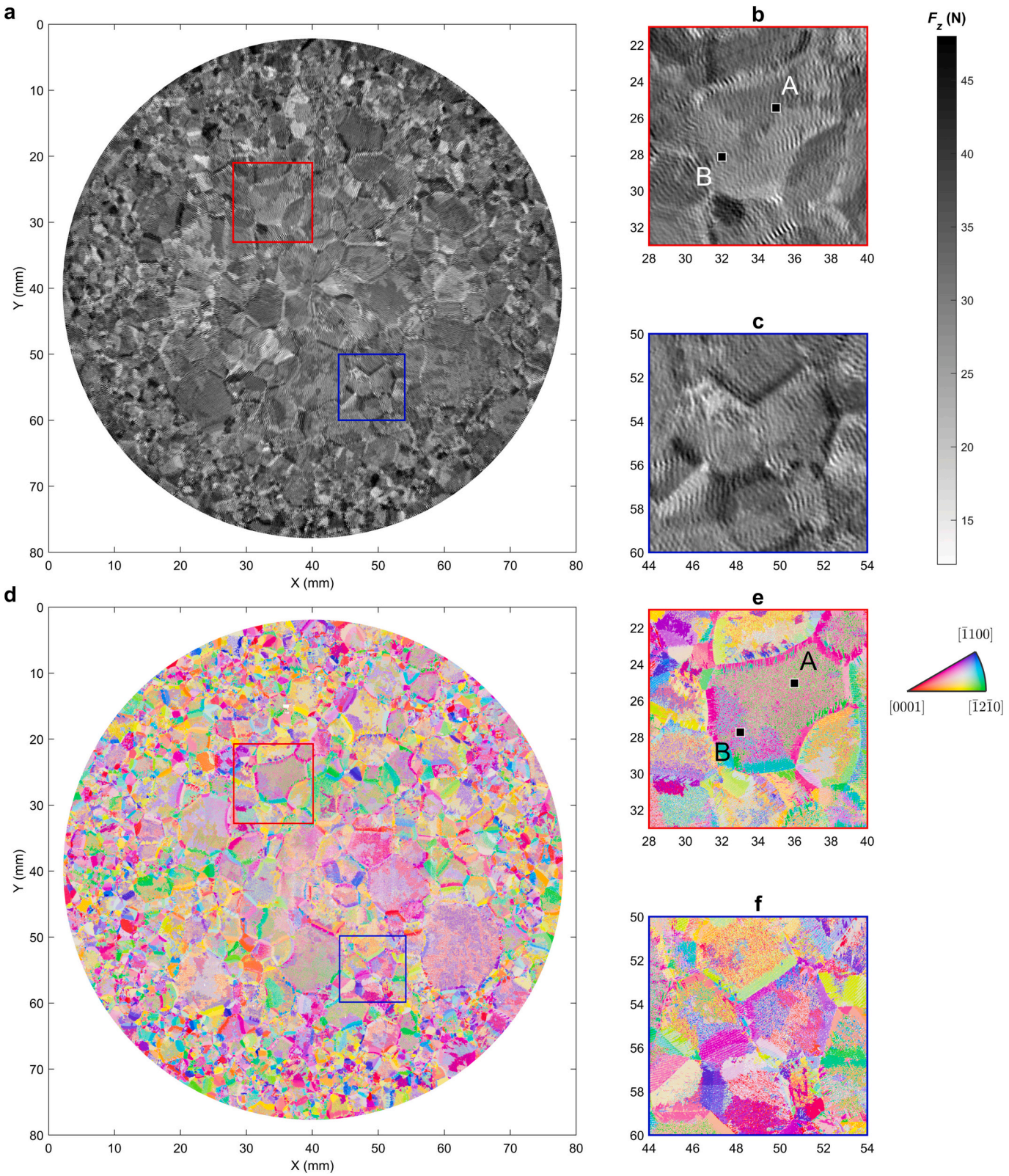

Fig. 6. Comparison of cutting force and crystallographic orientation data. **a,** Map of axial cutting force, F_z with highlighted regions showing microstructural features: **b,** A prior-β grain revealing variations in cutting force within the grain boundary suggesting the presence of α colony texture variation. **c,** A number of prior-β grains with high force regions distinguishable at grain boundaries suggesting the presence of grain boundary α (GB-α). **d,** An IPF map showing the α orientation of the same specimen acquired by EBSD analysis, with the same regions shown in **b,** and **c,** shown respectively in **e,** and **f.** (IPF maps have been colour-coded with respect to the specimen *z*-axis orientation).

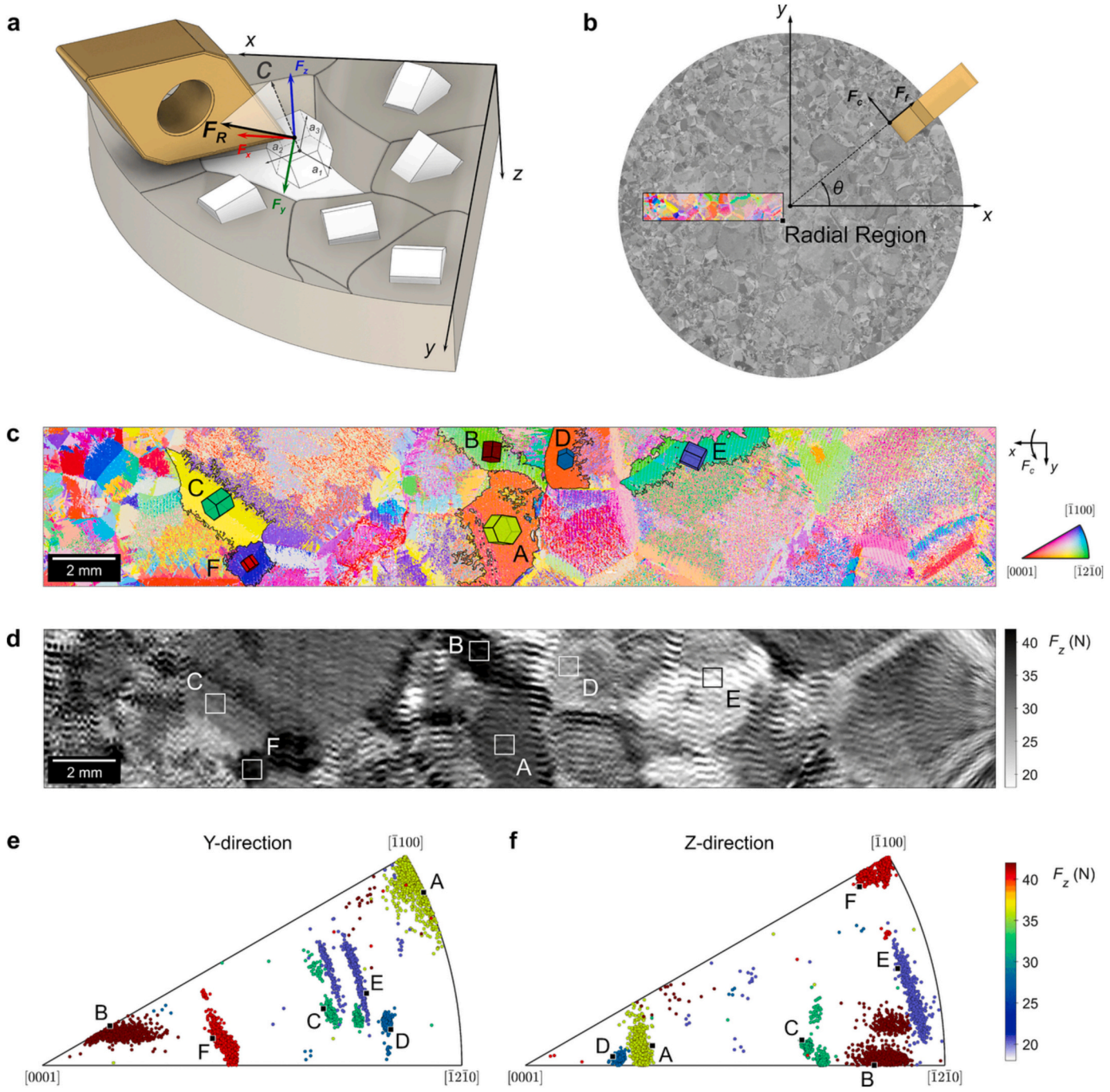

Fig. 7. Correlation between crystallographic orientation and measured cutting force. a, A schematic of the face turning operation indicating the cutting direction with respect to the hcp unit cell highlighting regions of the workpiece material which possess common crystallographic orientation. **b,** IPF map of the face turned surface showing the location of a radial region where the cutting direction and specimen *y*-direction are roughly aligned (i.e. $F_c \sim F_y$). **c,** IPF map showing α orientation within the radial region of interest highlighting grains A-F which display low levels of misorientation (<15°). **d,** Corresponding F_z cutting force map of the radial region showing common force regions associated with grains A-F. **e,** IPF scatter plot showing the orientation of indexed EBSD data points within grains A-F with respect to the specimen *y*-direction and **f,** with respect to the specimen *z*-direction. Data points are coloured based on the mean value of F_z taken from the common force regions shown in **d**. (In **b,** and **c,** the IPF maps have been colour-coded with respect to the specimen *z*-axis orientation).

β-transus temperature, such as the sintered Ti–6Al–4V used in this study, texture is developed as a result of the β→α phase transformation. Texture variants of α lamellae colonies develop following decomposition of the metastable β-phase and are formed according to the Burgers relationship [38], whereby respective close-packed planes of the parent β-phase and child α-phases are parallel (i.e., $\{110\}_\beta \parallel (0001)_\alpha$ and $\langle 1\bar{1}1\rangle_\beta \parallel \langle 2\bar{1}\bar{1}0\rangle_\alpha$) [28]. Due to this relationship, 12 possible α variants can form from an individual β grain, however typically stronger textures of fewer variant combinations form due to preferential nucleation of specific α variants [39]. The strong texture of these α-variant combinations, formed at neighbouring prior-β grains, is responsible for the heterogeneous response in cutting force, which has revealed the prior-β grain structure.

Two regions of interest have been identified to highlight higher resolution features that are displayed by the cutting force information. In Fig. 6b, the boundary of a prior-β grain is shown. This is of a similar size and morphology to that shown in the corresponding IPF map

(Fig. 6e). From the EBSD data, the α colonies within this prior-β grain can be identified to have two predominant textures. At the location labeled 'A', a combination of $(\bar{1}2\bar{1}0)$ and $(\bar{1}101)$ texture variants are present. This changes to a combination of $(\bar{1}100)$ and $(\bar{1}101)$ variants at 'B'. A correlation with this change in texture is displayed by the cutting force response, which shifts from higher forces at 'A' to lower forces at 'B'. This demonstrates that from analysis of the cutting force data, it is not only possible to distinguish the general prior-β grain structure, as previously reported by Suárez-Fernández et al. [11], but also identify changes in α colony texture present within the prior-β grain substructure.

Observations from a second region of interest, provided in Fig. 6c, shows regions of high cutting forces located along prior-β grain boundaries. These high forces correspond to GB-α which has nucleated at β grain boundaries during decomposition. This is a typical microstructural feature present in β-annealed Ti–6Al–4V and usually forms as either a continuous layer, or as parallel plates of a single texture variant [27]. Unlike α colonies formed within prior-β grains, the GB-α displays a single orientation variant, as shown by Fig. 6f. Therefore, machining stresses at regions of GB-α will interact with a stronger texture compared to stresses developed at α colonies inside prior-β grains. At these locations, interaction stresses will encounter the aggregate texture of a combination of α variants. In the case of the cutting forces response at the GB-α shown in Fig. 6c, this orientation has resulted in an increase in the force response, however, GB-α orientations which display a 'softer-to-machine' response can also be observed, such as those shown in Fig. 6b. This suggests that changes in the force response is a result of variation in the crystallographic cutting direction, rather than any changes in the local mechanical properties arising at GB-α.

3.2. Crystallographic orientation cutting force relationship

To correlate the relationship between crystallographic texture and cutting force, the cutting direction (i.e. the tangential F_c direction) and the crystallographic orientation must be defined by the same coordinate reference system. Whereas EBSD orientation data is defined in the Cartesian specimen coordinate system, the tangential direction of cutting motion varies as a function of its position. This means that for a grain of a given orientation, as defined by a single set of Euler angles, the crystallographic cutting direction would vary depending on the position of the grain on the specimen surface. Therefore, initial analysis of the crystallographic cutting force relationship has been performed for grains located within a radial region of the sample, as shown by Fig. 7. In this region, changes in are minimised and the cutting direction and specimen y-direction are roughly aligned (i.e. $F_c \sim F_y$). Therefore, the force response associated with different grains of the same orientation within this region should be roughly consistent, provided that a crystallographic cutting force relationship is detectable from the measured cutting force.

The analysis of the crystallographic cutting force relationship performed over the radial region is provided in Fig. 7. This relationship has been studied by considering the F_z response[1] of macrotextured regions (which will be referred to as 'grains') which display a single α texture variant and assuming single crystal behaviour for each grain based on their mean orientation, as depicted by the schematic in Fig. 7a. The six largest grains within the region (labeled A-F in the IPF provided in Fig. 7c) have selected for analysis. Each of these grains displays a unique orientation with respect to the local cutting direction. Grain boundaries have been determined by applying a misorientation threshold of 15° using the MTEX algorithm [40]. Fig. 7d shows a map of F_z for the radial area analysed. Regions of common magnitudes of F_z can be observed corresponding to grains A-F. For each grain, the mean value of F_z has been calculated from the sampled regions, A-F, shown in Fig. 7d. IPF scatter plots showing the EBSD orientation of the indexed data points for grains A-F with respect to the specimen y and z-directions are provided in Figs. 7e and f, respectively. Orientation data points are coloured based on the mean value of F_z corresponding to each grain to visualise the relationship between different orientations and their cutting force response.

[1] Analysis of crystallographic orientation with respect to the F_c response has not been performed due to the periodic banding in the signal which obscures the crystallographic cutting force relationship.

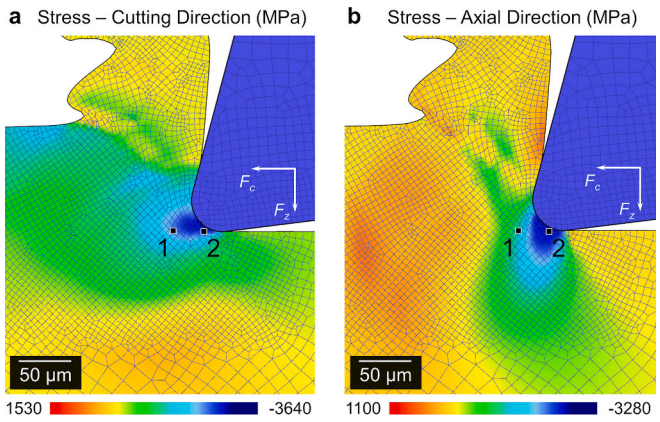

Fig. 8. Simulated FE stress distribution. **a,** Cutting directional and **b,** axial directional stresses developed ahead of the cutting edge. A change in the dominant stress direction occurs as material flows from 1 → 2, with material ahead of the tool at position 1 initially experiencing stresses primarily in the cutting direction, with an increase in axial stresses developing as material approaches the cutting edge at position 2.

Of the six grains selected, grain B displays the highest value of F_z. From the IPF scatter plot, this grain displays strong alignment of the [0001] and the y-direction, i.e. the c-axis is almost parallel to the local cutting direction. In this orientation, there is strong misalignment between the crystal a-axes and the cutting direction. The grain exerts high resistance to slip in the cutting direction, as the CRSS on $\{0001\}$ and $\{10\bar{1}0\}$ planes required to induce $\langle a \rangle$ slip is low with respect to the applied cutting directional stress. Other 'hard-to-cut' grains include grain F, which also displays a strong alignment between the [0001] and the cutting direction. The lowest force response can be observed at grain E, which shows strong alignment between the crystal a-axis and the local cutting direction. Both grains A and D display a similar orientation, with the (0001) plane aligned close to parallel to the machined surface. However, a dissimilar F_z response can be observed for the two grains. This can be explained by the differences in the rotation about the c-axis for the two grains, with grain D rotated such that it's a-axis is aligned more closely with the direction of cutting.

The observations for the grains selected suggests that a relationship between the crystallographic cutting direction and cutting force can be observed from the measured response. Variations in the resistance to basal and prismatic $\langle a \rangle$ slip in the cutting direction, due to changes in crystallographic orientation with respect to the cutting direction, are shown to be directly linked to the F_z response. Higher cutting forces correspond to stronger misalignment between the cutting direction and the crystal a-axes, whereas lower forces have been shown to correspond to better alignment. It is interesting that this relationship is observed from the cutting force response in the F_z direction, as the results show correlation between F_z and resistance to slip in the direction of cutting, i.e. normal to the z-direction. To better understand the relationship between the resistance to slip in the cutting direction and F_z, an orthogonal FE model representing the critical cutting parameters and cutting edge microgeometry was developed and is shown in Fig. 8. As shown by the model, plastic stresses are developed ahead of the tool, which induce slip in the workpiece as it approaches the cutting edge. Comparing the stress

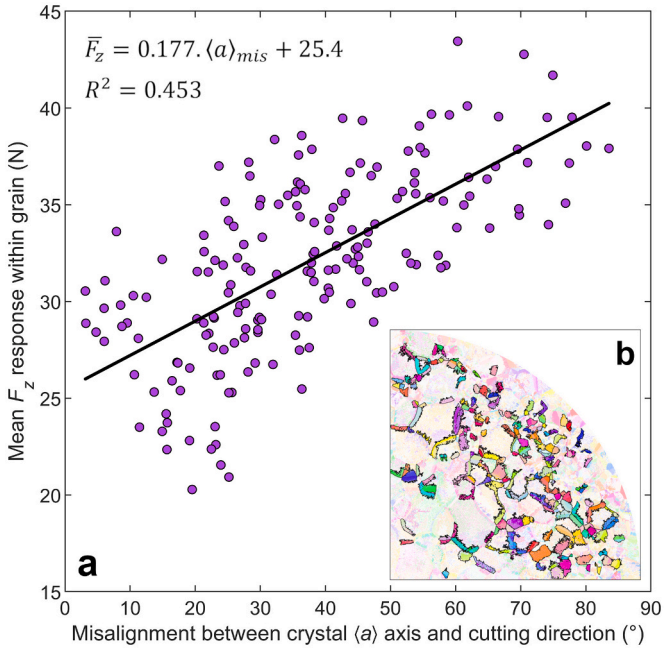

Fig. 9. a, Relationship between crystallographic ⟨a⟩ slip vector and cutting direction misalignment, $\langle a\rangle_{mis}$ vs. the F_z force response. Analysis has been performed based on the mean orientation for each grain and the mean F_z value, $\overline{F}_z$ within each corresponding grain boundary. **b,** Shows the 200 grains (or macrotextured regions) selected to perform the analysis. A misorientation threshold <15° was applied for grain boundary assignment.

distributions in the cutting and axial directions individually, shows that material ahead of the tool (position 1) initially experiences stresses predominantly in the cutting direction. As material approaches the cutting edge (position 2), it is subjected to increasing axial stresses. This suggests that material flowing towards the tool initially accommodates shear deformation in the direction of cutting, which is subsequently followed by further compressive strain in the *z*-direction, as it encounters the cutting edge. It can be postulated that for 'hard-to-cut' orientations, their high resistance to slip in the cutting direction means that they are subjected to less shear deformation ahead of the tool at position 1. This would mean that additional deformation in the *z*-direction is required as material encounters the cutting edge, such that material can flow beneath the tool during ploughing, resulting in an increase in the F_z response. This theory is supported by observations of the severe subsurface microstructural deformation, which occurs beneath the newly machined surface and shows different deformation characteristics of α lamallae based on their colony texture. Grain flow of α lamallae in the machined subsurface layer occurs either predominantly in a sweeping direction parallel to the direction of oncoming cutter motion (as shown by Fig. 10e), or with more discernible *z*-directional compression of the microstructure, which accompanies the swept grain (Fig. 10f). In the case where sweeping is more evident in the cutting direction (Fig. 10e), it is assumed that this microstructural response corresponds to a 'softer' texture. In this case, sweeping of the grain structure, as a result of shear deformation in the cutting direction, can be seen to reach a greater subsurface depth compared to the deformation morphology observed for the assumed 'harder' texture (Fig. 10e). For this 'hard' texture, the near surface region can be seen to have accommodated additional compressive strain near to the surface, which has been necessary to reach the total strain in the *z*-direction required for the material to flow beneath the tool.

Fig. 9 shows the relationship between the misalignment of the ⟨a⟩ slip vector and the local cutting direction vs. the F_z response. The misalignment angle, $\langle a\rangle_{mis}$ has been determined by calculation of the angular misalignment between the tangential cutting direction and the three crystal *a*-axes, and taking the lowest value. Analysis has been performed for 200 individual grains[2] based on their mean orientation and the mean F_z value, $\overline{F}_z$ within each corresponding grain boundary. The grains selected for the analysis are shown in Fig. 9b. Grains were selected which displayed a single dominant texture variant and which were of a size considerably larger than the predicted plastic interaction volume. The results show a positive correlation and support the previous observations that the F_z response is linked to the CRSS shear stress developed on ⟨a⟩ slip planes from applied stresses in the direction of cutting. It must be stressed that as grain size is reduced, the likelihood that they will display agreement with this relationship is diminished, as the volume of material interacting with stresses developed ahead of the cutting tool contains a greater number of individually oriented grains. This results in a force response which is associated with multiple texture variants contained within the stress interaction volume, and therefore, diminishes the influence of individual grain orientations on the measured cutting force.

Whilst the simple relationship in Fig. 8 demonstrates that is possible to make a general estimation regarding ⟨a⟩ vector misalignment for different macrotextured regions, it does not fully constrain the hcp crystallographic orientation in 3D space. This is because the relationship does not define crystallographic rotation around either the *a*-axis or cutting directional vectors. Through further work to establish the differences in the cutting force response associated with basal and prismatic ⟨a⟩ slip activation, it may possible to develop a model whereby crystallographic orientation could be defined more precisely by including additional terms for cutting force directions other than the passive component. To develop such a model, future work should focus on 2-D orthogonal cutting experiments and observe the interaction between forces measured in the cutting and passive directions when machining grains which favour deformation along different slip planes. Further refinement of this model which may be possible from 2-D orthogonal cutting experiments could focus on understanding the influence of neighbouring grain pairs, for example 'hard-to-soft' or 'hard-to-hard', combinations on the cutting force response.

It is also notable that the data displays considerable scatter. This can be attributed to the influence of forces unrelated to the effects of ploughing and crystallographic anisotropy on the measured F_z signal. Adiabatic shear banding and frictional effects occurring in the primary and secondary deformation zones also contribute to fluctuation in the F_z signal and introduce variability in the measurement, which cannot be accounted for by the crystallographic cutting force relationship. Future efforts to develop signal filtering techniques to reduce the influence of these factors may improve the model fit. Additionally, optimisation of cutting parameters and tool microgeometry to achieve cutting conditions whereby the contribution of macrotexture on the cutting force measurement is amplified compared to other influencing factors, may also prove to be advantageous.

To further understand the size of the interaction volume associated with machining stresses and its effect on the resolved features revealed by the cutting force maps, the simulated stress distribution determined from the orthogonal FE model has been shown in Fig. 10. A comparison between the simulated and measured forces in the F_c and F_z directions are provided in Fig. 10d and indicates some under-prediction of the simulated forces in both cases. This is expected to be due to the differences between the simulated orthogonal and experimental cutting mechanics due to the contribution of non-planar forces during the oblique face turning experiments. Additionally, the effects of increased rubbing, as the uncut chip thickness transitions from its maximum value of f_n to zero along the nose radius (0.40 mm) of the tool, also contributes to additional cutting forces. Despite these differences, the simulation is able to provide an approximate estimation of the size scale and shape of

[2] Here the term 'grain' is used to refer to a macrotextured region with a boundary misorientation threshold <15°, not individual α lamellae.

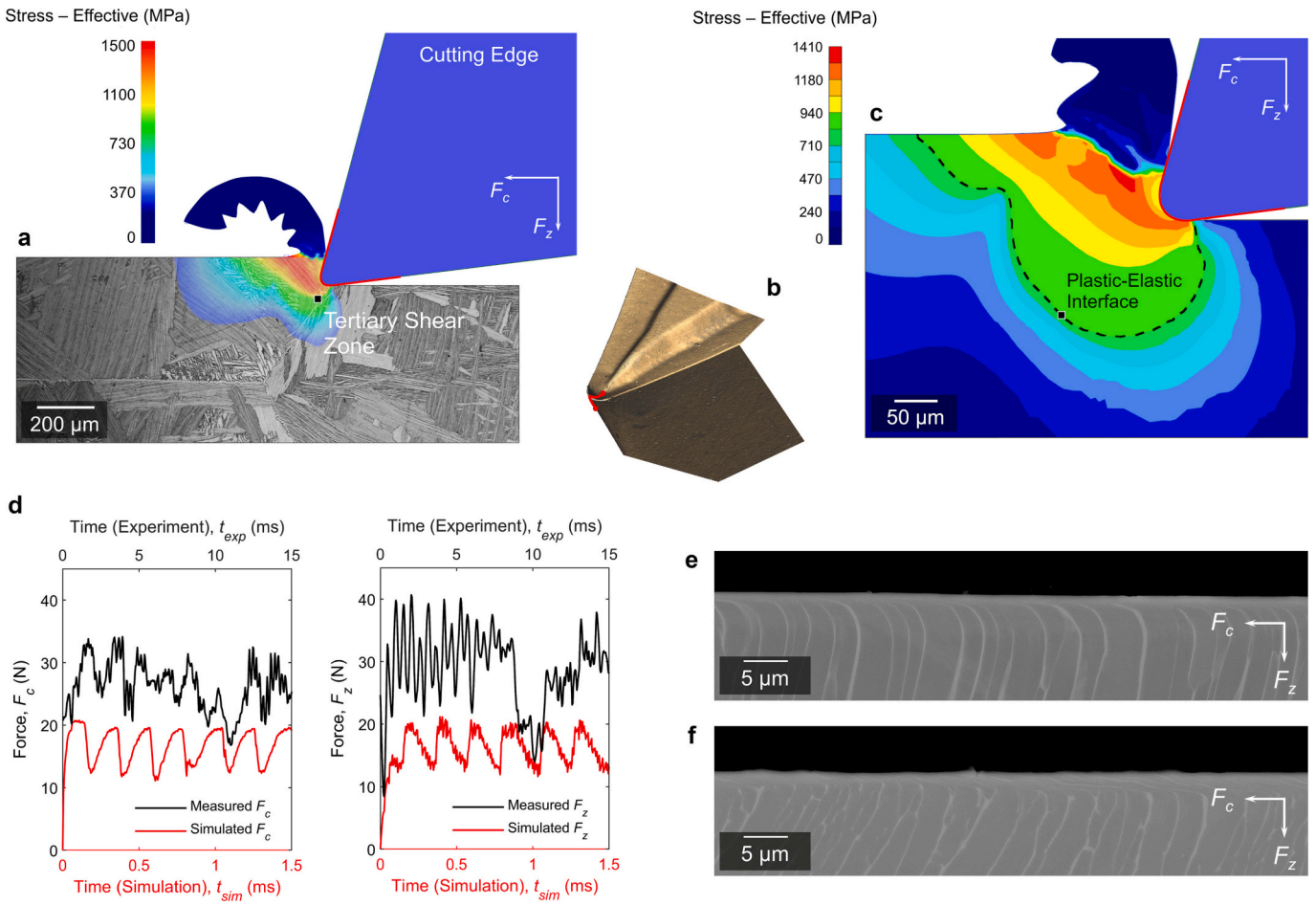

Fig. 10. FE orthogonal cutting simulation. **a,** The effective stress distribution indicating the size of the interaction volume with respect to the Ti–6Al–4V workpiece microstructure. **b,** A 3D scan representation of the WC-Co insert geometry highlighting the location of the 2D cutting edge profile used in the FEA orthogonal cutting simulations. **c,** A higher resolution image of the effective stress distribution indicating the interface between plastic and elastic stresses acting in the workpiece subsurface (σ_{yield} = 840 MPa). **d,** A comparison between measured cutting and axial cutting forces acquired during the face turning experiments with forces from the FEA orthogonal cutting simulation. **e,** A back-scattered electron (BSE) image of the workpiece subsurface following machining showing deformation of α lamellae indicating swept grain as a result of shear deformation taking place predominantly in the cutting direction and **f,** showing more severe deformation of the grain structure in the axial compressive direction.

the stress distribution, which is shown relative to the scale of the workpiece microstructure in Fig. 10a. The size of the plastic interaction volume, at which stresses acting above the isotropic yield point (σ_{yield} = 840 MPa) of the material is shown in Fig. 10b. This indicates a plastic interaction volume extending ~160 µm ahead of the tool in the cutting direction and ~ 130 µm in the axial direction. Based on an interaction volume of this scale, it is evident that it is not possible to resolve textures of microstructural features as small as individual α lamellae. However, evaluation of macro-scale regions larger than that of the interaction volume is possible, as the force response can be correlated directly to the material texture. For regions where the interaction volume encompasses multiple texture variants, such as the regions highlighted in Fig. 6b, the cutting force will relate to the aggregate response of the different textures present. Further work would be necessary to understand the force response associated with these texture variant combinations and ascertain the deformation behaviour of combined 'hard' and 'soft' textures under ploughing.

It is important to consider that the cutting force maps presented in this work are constructed from data points located at the moving position of the tool tip. Data points are representative of the cutting force measurement at this location, which has shown to correspond to a interaction stress volume which develops both ahead of, and beneath, the cutting tool. Therefore, the mapped forces will present information regarding workpiece texture slightly ahead of the captured force data point location, with the distance ahead of the data point varying depending on changes in the local yield strength of the material based on changes in it's texture. It is also notable that an elastic interaction with the workpiece material also occurs, with elastic stresses acting over an even larger volume than that of the plastic region, as shown in Fig. 10a. The effects of hcp crystal anisotropy on the elastic and shear moduli of titanium alloys are related to the alignment between the inclination of the crystal *c*-axis and the applied stress direction [27]. Greater misalignment between the *c*-axis and the applied stress results in a reduction in the elastic and shear moduli, which reaches its lowest value when the *c*-axis is perpendicular to the applied stress. If the elastic strain response of the material displayed similar tendencies to it's behaviour under plastic strain, as discussed previously, it could be argued that elastic anisostropy will also have a role on the crystallographic cutting force relationship. While this is true in part, the effects of elastic anisostropy would not account for differences in rotation of the crystal unit cell about the *c*-axis, which was shown to influence the cutting force response in the prior comparison made for grains A and D, Fig. 7. Therefore, it is expected that the effects of elastic anisostropy are of secondary importance to the materials plastic behaviour. Furthermore, as the elastic interaction volume is considerably larger than that of plastic stresses, it is of increased likelihood that the elastic response is

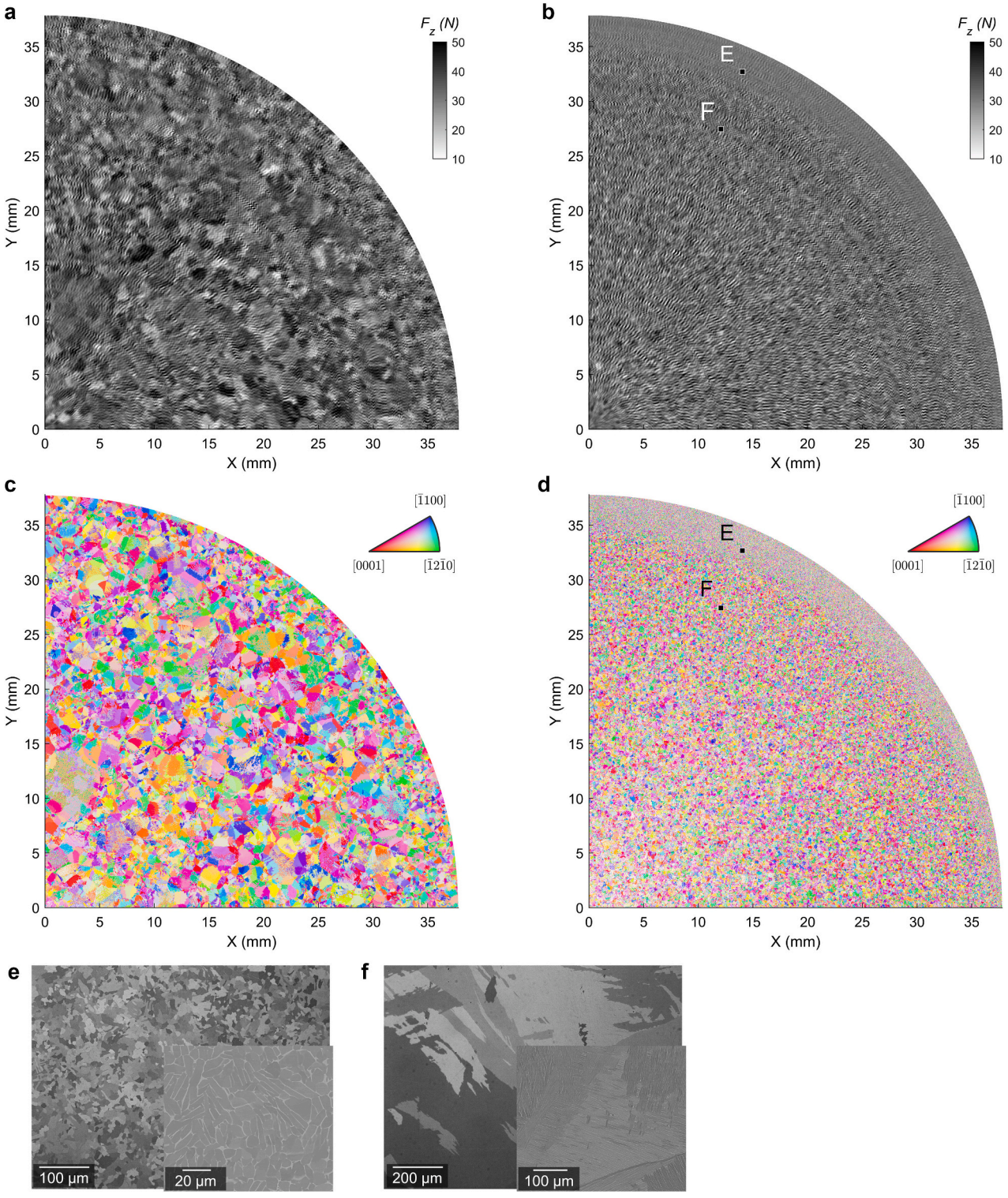

Fig. 11. Cutting force maps of FAST Ti–6Al–4V specimens featuring finer prior-β grain sizes. **a,** An F_z cutting force map of a FAST Ti–6Al–4V specimen consolidated at a dwell temperature of 1200 °C for 60 mins. **b,** An F_z cutting force map of a FAST Ti–6Al–4V specimen consolidated at a dwell temperature of 1050 °C for 10 mins showing a microstrucutre transitioning from a lamallar colony structure (labeled F) to a fine equiaxed structure (labeled E) when approaching the outer perimeter of the specimen. **c,** An IPF map of the specimen consolidated 1200 °C. **d,** An IPF map of the specimen consolidated 1050 °C highlighting the lamallar colony structure (F) and fine equiaxed structure (E) regions. **e,** Micrographs showing the morphology of the fine equiaxed FAST Ti–6Al–4V microstructure (E). **f,** Micrographs showing the morphology of the lamallar colony FAST Ti–6Al–4V microstructure (F). (In **c,** and **d,** the IPF maps have been colour-coded with respect to the specimen *z*-axis orientation).

averaged out over grains of various orientations and therefore, is less directly associated with smaller regions possessing a strong texture.

A final observation drawn from the orthogonal cutting model was that of periodicity in the cutting force due to the effect of adiabatic shear banding during chip formation. Chip serration from the simulation was shown to occur at a frequency of 5 kHz and therefore, of a similar order of magnitude to the 2 kHz periodic banding observed from the cutting force measurement. Discrepancies in these frequencies are most likely attributed to differences in material flow stress and strain rate data used in the simulation compared to the workpiece material used.

3.3. Minimum detectable size of microstructural features

To further demonstrate the microstructural characterisation capabilities achievable using spatially mapped cutting force data, two further Ti–6Al–4V specimens were machined using an identical methodology and are presented alongside their corresponding EBSD IPF maps in Fig. 11. These specimens were sintered from the same Ti–6Al–4V powder under identical processing conditions, however the dwell time and dwell temperatures were adjusted to achieve finer prior-β microstructures to assess the limitations of the technique as grain size is reduced with respect to the size of the machining stress interaction volume. Maps of F_z corresponding to specimens consolidated at 1200 °C for 60 mins and 1050 °C for 10 mins are shown in Figs. 11a and b, respectively. As the prior-β grain size is reduced to an approximate diameter of ~500 μm following consolidation at 1200 °C (Fig. 11a), the microstructure remains to be discernible from the mapped cutting forces, however the definition of prior-β grain boundaries is reduced compared to those observed for the larger grains presented previously in the discussion. For the specimen consolidated at 1050 °C, a transition from a fully transformed prior-β structure (location F, Fig. 11f) to a non-transformed, equiaxed α structure (location E, Fig. 11e) can be observed. This is due to processing temperatures at location E not reaching the β-transitional temperature, due to the thermal gradient along the specimen radial direction. This change in microstructure is depicted from the map of cutting force, which shows a homogeneous region with little fluctuation in cutting force approaching the specimen perimeter. Similar to individual α lamellae, the texture of the equiaxed α grain structure cannot be resolved as individual grains are of a size considerably smaller than that of the interaction stresses.

4. Conclusions

This article presents a new approach to texture characterisation which exploits the relationship between the changes in crystallographic cutting direction and fluctuations in the cutting force response. Through spatial mapping of cutting force measurement data acquired during face turning of Ti–6Al–4V, the characterisation of microstrucutral features such as the prior-β grain structure, GB-α, and colonies of similarly orientated α lamellae has shown to be possible. By the use of large area EBSD orientation data, a correlation between the misalignment of the crystallographic $\langle a \rangle$ slip vector with respect to the local cutting direction and the passive cutting force response has been established, showing an increase in cutting forces as this misalignment approaches 90°. These findings demonstrate that under ploughing, the CRSS developed from stresses in the direction of cutting on $\langle a \rangle$ slip systems are linked to the passive cutting force response. It has been hypothesised that for 'hard' textures, where the CRSS is lower, material is subjected to less shear deformation ahead of the tool. Therefore, additional strain is required in the passive direction, for material to flow beneath the cutting edge, resulting in an increase in the passive cutting force.

Industrially, these findings offer relevance, particularly to aero-engine manufacturers, who could potentially adopt such techniques in the future for the characterisation of microstructural features and macrozones in large, cold-dwell fatigue susceptible titanium alloy components, such as fan and compressor discs. Areas for future research deemed most pivotal would be to establish the differences in the cutting force response associated with basal and prismatic slip activation. This would make it possible to define crystal orientation without any ambiguity regarding its rotation about the *a*-axis. Additionally, further work to explore the role of cutting parameters and cutting edge microgeometry on the usefulness of the data obtained could be of particular interest to develop the technique further.

Application of this technique to crystalline structures other than hcp may also be possible, provided that their anisotropic deformation behaviour is sufficient to induce cutting force fluctuations that are detectable using similar instrumentation to that used in this study. Exploring the application of the technique for bcc and fcc materials presents an interesting area for future research.

CRediT authorship contribution statement

Thomas Childerhouse: Conceptualization, Formal analysis, Investigation, Methodology, Visualization, Writing – original draft, Writing – review & editing. **Oliver Levano-Blanch:** Conceptualization, Investigation, Methodology. **Xiaohan Zeng:** Formal analysis, Investigation, Methodology. **Joshua Taylor:** Formal analysis, Investigation, Data curation. **Dennis Premoli:** Data curation, Investigation. **Pete Crawforth:** Conceptualization, Resources, Supervision, Writing – review & editing, Project administration. **Rachid M'Saoubi:** Resources, Supervision, Writing – review & editing. **Martin Jackson:** Conceptualization, Funding acquisition, Project administration, Resources, Supervision, Writing – review & editing.

Declaration of Competing Interest

The authors declare no competing interests.

Data availability

Data will be made available on request.

Acknowledgments

TC and OLB were funded by the EPSRC through grants EP/S013377/1 and EP/T024992/1, respectively. DP and JT are funded through the EPSRC Centre for Doctoral Training in the Advanced Metallic Systems (EP/L016273/1). The authors would also like to thank Josh Priest at the Advanced Manufacturing Research Centre for his support in developing the orthogonal cutting FE model.

References

[1] E. Kuljanic, M. Sortino, TWEM, a method based on cutting forces—monitoring tool wear in face milling, Int. J. Mach. Tools Manuf. 45 (1) (2005) 29–34, https://doi.org/10.1016/j.ijmachtools.2004.06.016.

[2] A. Devillez, F. Schneider, S. Dominiak, D. Dudzinski, D. Larrouquere, Cutting forces and wear in dry machining of Inconel 718 with coated carbide tools, Wear 262 (7) (2007) 931–942, https://doi.org/10.1016/j.wear.2006.10.009.

[3] L. López de Lacalle, A. Lamikiz, J. Sánchez, M. Salgado, Toolpath selection based on the minimum deflection cutting forces in the programming of complex surfaces milling, Int. J. Mach. Tools Manuf. 47 (2) (2007) 388–400, https://doi.org/10.1016/j.ijmachtools.2006.03.010.

[4] E. Budak, Analytical models for high performance milling. Part I: Cutting forces, structural deformations and tolerance integrity, Int. J. Mach. Tools Manuf. 46 (12) (2006) 1478–1488, https://doi.org/10.1016/j.ijmachtools.2005.09.009.

[5] H. Miao, C. Wang, C. Li, W. Song, X. Zhang, M. Xu, Nonlinear dynamic modeling and vibration analysis of whole machine tool, Int. J. Mech. Sci. 245 (2023), 108122, https://doi.org/10.1016/j.ijmecsci.2023.108122.

[6] S. Cedergren, C. Frangoudis, A. Archenti, R. Pederson, G. Sjöberg, Influence of work material microstructure on vibrations when machining cast Ti-6Al-4V, Int. J. Adv. Manuf. Technol. 84 (2016) 2277–2291, https://doi.org/10.1007/s00170-015-7827-2.

[7] Y. Xu, S. Joseph, P. Karamched, K. Fox, D. Rugg, D. Dye, F. Dunne, Predicting dwell fatigue life in titanium alloys using modelling and experiment, Nat. Commun. 11 (11) (2020), https://doi.org/10.1038/s41467-020-19470-w.

[8] P. Tympel, T. Lindley, E. Saunders, M. Dixon, D. Dye, Macrozones and dwell fatigue crack initiation in Ti-6Al-4V, 2016, pp. 985–991, https://doi.org/10.1002/9781119296126.ch168.
[9] L. Yang, F. Dunne, The mechanistic link between macrozones and dwell fatigue in titanium alloys, Int. J. Fatigue 142 (10) (2020), https://doi.org/10.1016/j.ijfatigue.2020.105971.
[10] P. Crawforth, M. Jackson, S. Turner, B.P. Wynne, Linking machining response of titanium billet to upstream thermomechanical processing, in: Proceedings of the 13th World Conference on Titanium (2016), 2023, pp. 1649–1654, https://doi.org/10.1002/9781119296126.ch276.
[11] D. Suárez-Fernández, M. Jackson, P. Crawforth, K. Fox, B. Wynne, Using machining force feedback to quantify grain size in beta titanium, Materialia 13 (2020), 100856, https://doi.org/10.1016/j.mtla.2020.100856.
[12] D.S. Fernández, B.P. Wynne, P. Crawforth, M. Jackson, Titanium alloy microstructure fingerprint plots from in-process machining, Mater. Sci. Eng. A 811 (03) (2021), https://doi.org/10.1016/j.msea.2021.141074.
[13] S. Kieren-Ehses, L. Böhme, L. Morales-Rivas, J. Lösch, B. Kirsch, E. Kerscher, M. Kopnarski, J.C. Aurich, The influence of the crystallographic orientation when micro machining commercially pure titanium: a size effect, Precis. Eng. 72 (2021) 158–171, https://doi.org/10.1016/j.precisioneng.2021.04.007.
[14] B. Lawson, O. Ozdoganlar, Effects of crystallographic anistropy on orthogonal micromachining of single-crystal aluminum, ASME. J. Manuf. Sci. Eng. 130 (3) (2008) 03116, https://doi.org/10.1115/1.2917268.
[15] N. Kota, O.B. Ozdoganlar, Orthogonal machining of single-crystal and coarse-grained aluminum, J. Manuf. Process. 14 (2) (2012) 126–134, micro and Nano Manufacturing, https://doi.org/10.1016/j.jmapro.2012.01.002.
[16] M. Sato, Y. Kato, K. Tsutiya, S. Aoki, Effects of crystal orientation on the cutting mechanism of aluninum single crystal, Bull. JSME 24 (196) (1981) 1864–1870, https://doi.org/10.1299/jsme1958.24.1864.
[17] E. Schmid, W. Boas, Crystal Plasticity: With Special Reference to Metals, Springer Berlin Heidelberg, 1935, https://doi.org/10.1007/978-3-662-34532-0.
[18] E. Demir, A method to include plastic anisotropy to orthogonal micromachining of fcc single crystals, Int. J. Adv. Manuf. Technol. 43 (2009) 474–481, https://doi.org/10.1007/s00170-008-1738-4.
[19] W. Lee, M. Zhou, A theoretical analysis of the effect of crystallographic orientation on chip formation in micromachining, Int. J. Mach. Tools Manuf. 33 (3) (1993) 439–447, https://doi.org/10.1016/0890-6955(93)90050-5.
[20] K. Ueda, K. Iwata, K. Nakayama, Chip formation mechanism in single crystal cutting of β-brass, CIRP Ann. 29 (1) (1980) 41–46, https://doi.org/10.1016/S0007-8506(07)61292-X.
[21] Z. Yuan, W. Lee, Y. Yao, M. Zhou, Effect of crystallographic orientation on cutting forces and surface quality in diamond cutting of single crystal, CIRP Ann. 43 (1) (1994) 39–42, https://doi.org/10.1016/S0007-8506(07)62159-3.
[22] M. Zhou, B.K.A. Ngoi, Effect of tool and workpiece anisotropy on microcutting processes, Proc. Inst. Mech. Eng. B J. Eng. Manuf. 215 (1) (2001) 13–19, https://doi.org/10.1243/0954405011515091.
[23] E. Demir, A Taylor-based plasticity model for orthogonal machining of single-crystal FCC materials including frictional effects, Int. J. Adv. Manuf. Technol. 40 (1) (2009) 847–856, https://doi.org/10.1007/s00170-008-1409-5.
[24] N. Kota, O.B. Ozdoganlar, A model-based analysis of orthogonal cutting for single-crystal fcc metals including crystallographic anisotropy, Mach. Sci. Technol. 14 (1) (2010) 102–127, https://doi.org/10.1080/10910340903586517.
[25] E. Demir, C. Mercan, A physics-based single crystal plasticity model for crystal orientation and length scale dependence of machining response, Int. J. Mach. Tools Manuf. 134 (2018) 25–41, https://doi.org/10.1016/j.ijmachtools.2018.06.004.
[26] N.S. Weston, B. Thomas, M. Jackson, Processing metal powders via field assisted sintering technology (FAST): a critical review, Mater. Sci. Technol. 35 (11) (2019) 1306–1328, https://doi.org/10.1080/02670836.2019.1620538.
[27] G. Lütjering, J. Williams, Titanium, Engineering Materials and Processes, Springer Berlin Heidelberg, 2007.
[28] G.A. Sargent, K.T. Kinsel, A.L. Pilchak, A.A. Salem, S.L. Semiatin, Variant selection during cooling after beta annealing of Ti-6Al-4V ingot material, Metall. Mater. Trans. A 43 (1) (2012) 3570–3585, https://doi.org/10.1007/s11661-012-1245-y.
[29] M. Calamaz, D. Coupard, F. Girot, A new material model for 2D numerical simulation of serrated chip formation when machining titanium alloy Ti–6Al–4V, Int. J. Mach. Tools Manuf. 48 (3) (2008) 275–288, https://doi.org/10.1016/j.ijmachtools.2007.10.014.
[30] D. Umbrello, Finite element simulation of conventional and high speed machining of Ti6Al4V alloy, J. Mater. Process. Technol. 196 (1) (2008) 79–87, https://doi.org/10.1016/j.jmatprotec.2007.05.007.
[31] W.-S. Lee, C.-F. Lin, High-temperature deformation behaviour of Ti6Al4V alloy evaluated by high strain-rate compression tests, J. Mater. Process. Technol. 75 (1) (1998) 127–136, https://doi.org/10.1016/S0924-0136(97)00302-6.
[32] E. El-Magd, C. Treppmann, Simulation of chip root formation at high cutting rates by means of Split-Hopkinson Bar Test, Materialprüfung/Materials Testing 41 (11–12) (1999) 457–460.
[33] E. El-Magd, C. Treppmann, Mechanical behaviour of materials at high strain rates, Scientific Fundamentals of HSC (2001) 113–136.
[34] E. El-Magd, C. Treppmann, M. Korthäuer, Constitutive modelling of CK45N, AlZnMgCu1.5 and Ti-6Al-4V in a wide range of strain rate and temperature, J. Phys. IV France 110 (2003) 141–146, https://doi.org/10.1051/jp4:20020684.
[35] F. Bachmann, R. Hielscher, H. Schaeben, Texture analysis with MTEX – Free and open source software toolbox, in: Texture and Anisotropy of Polycrystals III vol. 160 of Solid State Phenomena, Trans Tech Publications Ltd, 2010, pp. 63–68, https://doi.org/10.4028/www.scientific.net/SSP.160.63.
[36] P. Basuray, B. Misra, G. Lal, Transition from ploughing to cutting during machining with blunt tools, Wear 43 (3) (1977) 341–349, https://doi.org/10.1016/0043-1648(77)90130-2.
[37] D.J. Waldorf, R.E. DeVor, S.G. Kapoor, An evaluation of ploughing models for orthogonal machining, J. Manuf. Sci. Eng. 121 (4) (1999) 550–558, https://doi.org/10.1115/1.2833050.
[38] W. Burgers, On the process of transition of the cubic-body-centered modification into the hexagonal-close-packed modification of zirconium, Physica 1 (7) (1934) 561–586, https://doi.org/10.1016/S0031-8914(34)80244-3.
[39] N. Stanford, P. Bate, Crystallographic variant selection in Ti–6Al–4V, Acta Mater. 52 (17) (2004) 5215–5224, https://doi.org/10.1016/j.actamat.2004.07.034.
[40] F. Bachmann, R. Hielscher, H. Schaeben, Grain detection from 2d and 3d EBSD data—specification of the MTEX algorithm, Ultramicroscopy 111 (12) (2011) 1720–1733, https://doi.org/10.1016/j.ultramic.2011.08.002.